FR9100180

I.P.N. BP n°1 – 91406 ORSAY

institut de physique nucléaire CNRS - IN2P3 - UNIVERSITÉ PARIS - SUD

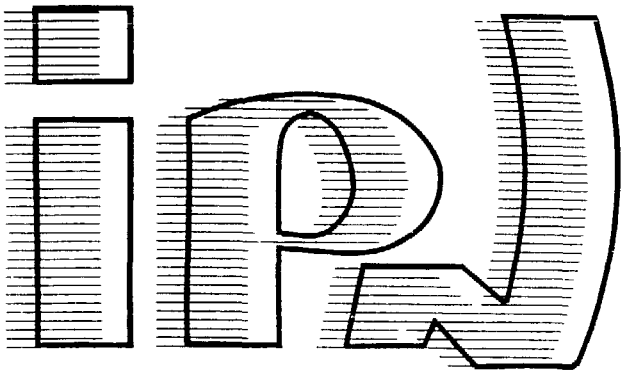

IPNO-DRE-90-10

A DOUBLE ZERO-DISPERSION MAGNETIC SPECTROMETER USED IN A TELESCOPIC MODE FOR VERY FORWARD HEAVY IONS STUDIES.

Ch.O. BACRI, P. ROUSSEL

A DOUBLE-ZERO-DISPERSION-MAGNETIC SPECTROMETER USED IN A TELESCOPIC MODE FOR VERY FORWARD HEAVY IONS STUDIES

Ch.O. BACRI and P. ROUSSEL
Institut de Physique Nucléaire, 91406 - Orsay Cedex, France

Abstract

An original method based on the use of a double magnetic spectrometer in a telescopic mode is proposed for the studies of heavy ions collisions both at very forward angles and for magnetic rigidities close to that of the beam. It consists in the direct measurement of angular distributions on doubly - $B\rho$ and angle - sorted events. The method has been tested on the LISE spectrometer at GANIL with a 44 MeV/A ^{40}Ar beam impinging on C, Al, Ni and Au targets. Milli-radian angular accuracy have been obtained at magnetic rigidities as close as 0,9977 of that of the beam.

Magnetic spectrometers which provide accurate energy measurements (after identification) on charged reaction products are also very efficient to perform $B\rho$ sorting, allowing the elimination of abundant uninteresting products. This is the case for the beam in one of its charge state after the target, when the spectrometer is set at or close to "0°", the direction of the beam. However, a single step magnetic sorting has been shown to become not sufficient enough when one needs to work both very close to the magnetic rigidity of the beam and at very small angles (for simplicity, "close to the beam"). Besides, small angles have taken an increasing importance with the acceleration of heavier ions at higher energies (30 to 100 MeV/A and above). A dominant part of the reaction products are indeed "focused" in the forward direction. The semi-classical grazing angle θ_{gr}^{lab} gives an evaluation of the useful angular range (Table 1). On the other hand, the inverse of the grazing momentum l_{gr} is also indicated in Table 1 and gives a rough idea of the minimum angular size of the structures which may result from an ondulatory behaviour in the collision. This minimum size is related to the required experimental angular accuracy.

The problems encountered in "close to the beam" measurements are best examined in the $B\rho$-θ phase space, the study of which will be first presented. Next, we will show how a zero-dispersion double spectrometer used in a telescopic mode can be a way to solve some of the problems. Finaly, we will present the adaptation of this method to the LISE spectrometer at GANIL and exhibit its efficiency through results obtained in an experiment with a 44 MeV/A ^{40}Ar beam on C, Al, Ni and Au targets.

1. THE $B\rho$-θ PHASE SPACE

Elastic scattering on light target contaminants, elastic scattering on entrance slits and ghost beams bring the main limitations when performing measurements "close to the beam". Any studied nuclear reaction as well as the above mentioned spurious phenomena are caracterised by a given correlation in the $B\rho$-θ plane and by a given yield for each point of this plane. Such a plot is given for the two first of them on figure 1, for the typical case of an ^{40}Ar beam at 44 MeV/A on different targets. The $B\rho$ axis is scaled by its ratio to that of the beam (right scale) and by the absolute kinetic energy loss (left scale). The indicated yield is that of the Coulomb scattering given as the fraction of the incident beam, found per angular unit (milliradian). The Gold and Aluminium thicknesses are those of the used targets, while the much

thinner proton and Carbon ones are those of possible contaminants (1 atom per 1000 of Aluminium).

As expected, the behaviour of the correlation is strongly dependant on the target mass, the lighter the target, the steeper the correlation. With the realistically chosen windows, the proton correlation is nearly vertical while the gold one is nearly flat. A single $B\rho$ shielding 1,4 ‰ wide corresponding to 5 MeV (the horizontal dashed region on figure 1) can actually eliminate all the elastically scattered beam on Gold, in the studied angular range. With Aluminium, the angular limit is still high enough ($\simeq$ 40 mr) but it drops to 8 mr for the hydrogen contaminant, bringing a fraction of $\simeq 2.10^{-8}$ of the beam in the active window. For an incident beam of 10^{12} pps (particle per second), this corresponds to 2.10^{4} spurious events per second.

Such a prohibitive counting rate can be strongly decreased if an angular shield (the vertical dashed region on figure 1) from about 7 mr to 10 mr, for instance, is added. It can even be eliminated within the selected $B\rho$ window if the angular upper limit of the shield is increased. An equivalent operation would be needed for the Carbon contaminant unless its amount is substantially decreased (which is more feasible than for Hydrogen). This "double shielding" makes available for measurements this low energy loss - low angular range part of the dynamics.

One could think to perform the angular sorting by the mean of entrance slits but, apart from the fact that they would not define an accurate angular range due to the beam spot size on the target, it is very important to notice that these slits would be submitted to a very important bombardment of particles scattered by the target : more than 10^{8} events per second and per mr for the Aluminium or the Gold target* . They would therefore become a prohibitive source of doubly scattered particles, as actually found in such experiment.

A more complete study of the repartition of reaction products and of the beam after the target in the $B\rho$-θ plane requires the angular and energy straggling in the target to be taken into account.

---

* As well known, the Coulomb scattering cross section $d\sigma/d\theta$ evolves with the incident beam (A_1, Z_1, $E_1=A_1\xi_i$), the target (A_2,Z_2) and the (assumed small) laboratory angle as: $(Z_1Z_2/E_1)^2\ \theta^{-3}$. The yield is proportional to e/A_2 ($mg.cm^{-2}.amu^{-1}$).

The angular straggling is due to elastic collisions of the projectile with the target nuclei shielded by electrons ; it has been thouroughly studied by Meyer [1] for low energy and later by Sigmund and Winterbon [2] and Langevin [3] for higher energy ; these studies were extended by J. Hérault [4] to the GANIL energies. As for the energy straggling, it is due to the statistical fluctuations of the beam slowing down by the target electrons [4-8]. As far as multiple scattering is concerned, i.e. at small angles, the two phenomena are independant (no correlation). At large angles, the fully correlated Rutherford single scattering become predominant* . But even there, this single scattering is necessarily accompanied by the angular and energy spreading which preceeds or follows ; the appropriate convolution has then to be proceeded to. The intermediate region ($\theta_{1/2} < \theta < \theta_R$, see table 2) is more complex. It is bounded to uninterestingly small angles for thin targets ($\leq$ 1 mg/cm^2) but it comes into the used angular range for thicker targets.

Figure 2 shows the contour map of the found phase space of the beam after multiple scattering of a 44 MeV/A impinging on a 8.1 mg/cm^2 Al target. It gives the probability of a beam ion to be emitted between the cones defined by the half angle θ and $\theta+d\theta$ and with an energy loss t ; each curve is separated from its neighbour by a factor 10. The plotted function is normalized to one at $\theta=0$ and t=0. The kinematical correlations for the proton, the Carbon and the Gold targets are also indicated. The curve labelled 10^{-14} is considered as the limit above which the straggling effects have disappeared. For 10^{12} incident particles per second, it indeed corresponds to a counting rate of 10^{-2} events per second. The distribution is larger when the target is heavier and thicker. But usually, the energy straggling due to the target can be neglected for practical cases at GANIL, except for low excitation inelastic measurements. At last, a typical emittance of a beam is indicated (dashed part of the figure). Once more, we can see how an angular shield could eliminate its effects.

---

*It is possible to define an angle θ_R which separates these two regimes [SIG74,HER88,BAC89] : for $\theta<\theta_R$, multiple scattering is the main phenomena.

2. THE TELESCOPIC MODE METHOD

The notations of the TRANSPORT code [9], a short abstract of which can be found in the Appendix, will be used in the following.

To proceed to the Bρ sorting, one needs to establish, together with a linear dispersion ($R_{16} \neq 0$), a point to point focusing between the target and the so-called "focal plane" where the slits and shields are situated*. This is obtained by the use of a magnetic dipole in conjonction with the use of pole face rotations, and quadrupoles.

To be effective, the second (angular) sorting has to be done independantly of the magnetic rigidity, that is, the whole system has to be made achromatic at that point (we will come back to this point). So, a second magnetic dipole** is needed to reconcentrate the selected reaction products.

Usually, angular sorting is done by the use of the spectrometer entrance slits and/or that of the beam catcher (Faraday cup) ; we have already seen

---

* If the only beam is to be eliminated, the corresponding shield will be better situated at the waist which is found between the point-to-point and the parallel-to-point focusses. But for the studied scattered particles, the eliminated Bρ zone will consequently depend on the emission angle of that particles.

** A quadrupole could locally cancel the linear dispersion ; but if R_{11} is also to be zero, in order to have no dependance on the beam size at the target, the need for the second dipole comes practically from the need for a large resolving power at the dispersive focus.

- At the dispersive focus F (Bρ sorting), a large resolving power leads to $\int_0^F R_{12}\, d\alpha$ large (see appendix).
- At the achromatic point A (angular sorting) , $R_{11}^A = 0$ and $R_{16}^A = 0$;

then, $\int_0^A R_{11}\, d\alpha = 0$.

These two conditions are difficult to obtain together without a second dipole (i.e. when $d\alpha = 0$ between F and A).

Moreover, the second dipole can also eliminate all the products scattered on the Bρ sorting slits.

this method is not feasible for the small angles region. Besides, angular measurements are the most often performed by ray-tracing techniques which do not allow to select or to eliminate particles with respect to their emission angle. On the contrary, if the final (angular) sorting plane is set in the conjugate plane of the infinity, a parallel to point relationship is established between the target and the final plane (telescopic mode) : one emission angle is then related by a one to one correspondance to a position on that plane independantly of the particle position at the target and both accurate angular sorting and accurate angular measurements are made available (see Fig. 3). All other measurements (ΔE-E, time of flight...) can then be performed on these doubly sorted event (see Fig. 4).

The only linear achromaticity ($R_{16} = 0$) is needed (see **) in that plane while the remaining angular dispersion (R_{26}) could be used to measure the magnetic rigidity of the doubly sorted events [10].

The main limitation for this method comes from the beam emittance through the Liouville theorem : a good $B\rho$ sorting requires x_i^{max} to be small (see remark i of the Appendix) while a good angular sorting requires θ_1^{max} to be small. But, the Liouville theorem keeps constant the emittance : $x_i^{max}\ \theta_1^{max} = \varepsilon_H$ at a waist (see A3 and A4 of the Appendix). A compromise between these two conditions has then to be found. However, small angle cross sections are expected to be large when this telescopic mode is needed and a reduction of the beam emittance so as to have both x_1^{max} and θ_1^{max} small enough can solve the problem without leading to very small counting rates.

3. ADAPTATION TO THE LISE SPECTROMETER OF GANIL. THE EXPERIMENTS AND THE RESULTS.

To test the method, the telescopic mode has been set up on the LISE spectrometer [11] at GANIL [12]. As it was designed to work in a point to point configuration, this adaptation has led to some limitations (Fig. 5).

The first one concerns the value of the angular dispersion R_{26} which could not be given high enough a value to allow $B\rho$ measurement from ray-tracing techniques, and which was finally set to zero. The $B\rho$ measurement was then performed by the $B\rho$ sorting itself (a total $B\rho$ aperture of 0.75 % max was used).

The obtained focal lengths ranged from 1.7 to 10 meters, that is R_{12} and R_{34} from 0.17 to 1.0 cm/mr. The 0.17 value was the most often used. Second order matrix elements are listed in table 3 and lead us to reduce the beam emittance. The transport matrix and typical beam enveloppes are displayed on Fig. 6. Finally, the maximum aperture of the spectrometer is close to the angle with which the first quadrupole is seen from the target that is about ± 30 mr.

The experiments were performed with a 44 MeV/A ^{40}Ar beam (50 to 200 nAe) impinging on C, Al, Ni and Au thin targets (< 10 mg/cm^2). The telescopic mode of the spectrometer was first tested and the angular calibration given by setting a test pattern 600 mm away from the target. Fig. 7 shows the latter and its image in the non dispersive detector plane* . The angular aperture of the system was also deduced from this image and found from ± 28 mr low efficiency down to ± 20 mr full efficiency in the Y plane (angle φ). The values are far enough smaller than the expected ones and although no clear explanation could be found for this difference, it has been assumed that it comes from a larger sensitivity to misalignements than in the usual setting of LISE.

The method has been tested by actually setting the system at 0° and as close as 2.3 ‰ of the beam's rigidity. Fig. 8 gives some results of such a study for the ^{197}Au target. On part a, the 2-dimensional ΔE versus time of flight (TOF) scatter plot is given for $0 \leq \theta \leq 7$ mr and for $0.9671 \leq \frac{B\rho}{B\rho_0} \leq 0.9754$ (left) and $0.9892 \leq \frac{B\rho}{B\rho_0} \leq 0.9977$ (right). The increasing importance of the ^{40}Ar counting rate can be noticed when approaching to the beam magnetic rigidity $B\rho_0$. Note also the occurence of some "noise" for the identification. The full range angular distribution in the Y plane (θ integrated) of the events having the ^{40}Ar time of flight is given on part b. By shielding the very central angular region of the beam ($\simeq$ ± 3 mr) (part c) the counting rate can be decreased by more than one order of magnitude, and identification is strongly improved for the selected events.The method makes possible measurements both at 0° and at 2.3 ‰ of the beam's rigidity, that is with an excitation energy in the elastic channel of $\simeq$ 8 MeV. The angular sorting, done here

---

* We can notice the effect of the $(y/\theta^2\varphi)$ aberration in the Y plane, that is the image of a straight slit becomes parabolic.

during the off-line analysis, could of course be done by the use of shields or screens or a hole in the detector in order to actually reduce the counting rates.

Angular distributions of all the produced fragments have been measured with such a set up, for magnetic rigidities from 0.75 to 1.2 of that of the beam. The complete study will be published elsewhere, and a study of the obtained velocity spectra at 0°, in the framework of the projectile fragmentation can be found in ref [13]. A sample of angular distributions is given here on Fig. 9. It shows different behaviours (forward peaked, no-forward peaked) of ^{40}Ar (dashed lines) and ^{38}Cl (dotted lines), when they are produced by a Ni target, at $0.9681 \leq B\rho/B\rho_0 \leq 0.9754$.

4. CONCLUSION

An original method based on the use of a double magnetic spectrometer is proposed for the studies of heavy-ions collisions at very forward angles. It consists on performing two sequential sorting, a $B\rho$ one in the dispersive plane after the first dipole and an angular one at the end of the two-dipoles system set in a zero-dispersion-telescopic-mode. It has been tested on the LISE spectrometer of GANIL with a 44 MeV/A ^{40}Ar beam and C, Al, Ni and Au targets. Despite some limitations due to the necessary adaptation of the method to LISE, it has allowed to obtain very accurate angular distributions at and around 0°. A sample of them is shown (a more complete study of the results will be published elsewhere) for magnetic rigidities as close as 0,9977 of that of the beam corresponding to an excitation energy down to 8 MeV in the incident channel.

R. Anne* is acknowledged for his contribution to the setting on the LISE spectrometer, J.C. Jacmart for his permanent support for this study, both of them and M. Bernas, Y. Blumenfeld, F. Clapier, H. Gauvin, J. Hérault, A. Latimier, P. Lelong, F. Pougheon, J.L. Sida, C. Stéphan and T. Suomijarvi for their participation to the experiments at GANIL.

* GANIL, Caen

APPENDIX : The TRANSPORT notations

A trajectory is represented, at any specified position s by a vector whose components are, in the horizontal plane (resp. the vertical plane), the position x (y), the angle θ (φ) and the momentum p, with respect to the reference trajectory, i.e. the central path. In a "classical" beam line (only dipoles, quadrupoles and sextupoles elements), the evolution of these coordinates from I to F is described by a matrix R :

$$\begin{pmatrix} x_F \\ \theta_F \\ \delta_F \end{pmatrix} = \begin{pmatrix} R_{11} & R_{12} & R_{16} \\ R_{21} & R_{22} & R_{26} \\ 0 & 0 & 1 \end{pmatrix} \begin{pmatrix} x_I \\ \theta_I \\ \delta_I \end{pmatrix} \quad \text{in the horizontal plane}$$

where $\delta = \frac{\Delta p}{P}$, and

$$\begin{pmatrix} y_F \\ \varphi_F \end{pmatrix} = \begin{pmatrix} R_{33} & R_{34} \\ R_{43} & R_{44} \end{pmatrix} \begin{pmatrix} y_I \\ \varphi_I \end{pmatrix} \quad \text{in the vertical plane.}$$

R_{11} (R_{33}) is the linear magnification in the horizontal (vertical) plane, R_{22} (R_{44}) the angular magnification, R_{21} (R_{43}) the inverse of the focal length, R_{12} (R_{34}) the focal length, R_{16} the dispersion, and R_{26} the angular dispersion.

The Liouville theorem states that if no acceleration occurs in a beam line, the total emittance of the beam is conserved. In terms of matrix elements, this is expressed by :

$$R_{11} R_{22} - R_{21} R_{12} = 1 \qquad (A1)$$
$$R_{33} R_{44} - R_{43} R_{34} = 1 \qquad (A2)$$

In terms of spot size for an erected ellipse, this is expressed by :

$$x_1^{max} \theta_1^{max} = \text{cte} \qquad \text{for the horizontal plane (A3)}$$
$$y_1^{max} \varphi_1^{max} = \text{cte} \qquad \text{for the vertical plane (A4).}$$

Moreover, these matrix elements are related by the following relations (where R_{16}^{AB} denotes the matrix element R_{16} from point A to point B).

$$R_{16}^{AB} = R_{12}^{AB} \int_A^B R_{11}\, d\alpha - R_{11}^{AB} \int_A^B R_{12}\, d\alpha \qquad (A5)$$

$$R_{26}^{AB} = R_{22}^{AB} \int_A^B R_{11}\, d\alpha - R_{21}^{AB} \int_A^B R_{12}\, d\alpha \qquad (A6)$$

$$R_{51}^{AB} = \int_A^B R_{11}\, d\alpha \quad ; \quad R_{52}^{AB} = \int_A^B R_{12}\, d\alpha \qquad (A7)$$

where $d\alpha$ is the bending angle corresponding to the central path. $d\alpha = 0$ outside of a dipole.

These relations lead to important remarks when one of the matrix elements is set to 0.

i) $R_{12} = 0$: dispersive focus : $x_f = R_{11}\, x_i + R_{16}\, \delta_i$.

Two object caracterized by $\delta_i=0$ and $\delta_i\neq0$ can be resolved if $R_{16}\, \delta_i \geq R_{11}\, x_i$; δ_i can be as small as R_{16}/R_{11} is large. This ratio $\frac{R_{16}}{R_{11}} = - \int R_{21}\, d\alpha = - R_{52}$ (see A5) is the *resolving power* of the line. Notice that a good resolution needs x_i to be small, that is a small spot size of the beam on the target.

ii) $R_{11} = 0$ and $R_{16} = 0$: parallel to point relationship.

One can deduce from (A1) and (A5) : $R_{51} = \int R_{11}\, d\alpha = 0$.

References

[1] L. Meyer, Phys. Stat. Sol. 44 (1971) 253.

[2] P. Sigmund and K.B. Winterbon, Nucl. Instr. and Meth. 119 (1974) 541.

[3] M. Langevin, IPNO-Ph.N-81-09.

[4] J. Hérault, Thèse d'Université, IPNO-DRE-88-25.

[5] P.V. Vavilov, JETP, vol. 5, n° 4 (1957) 749.

[6] F. Besenbacher, Nucl. Instr. and Meth. 168 (1980) 1.

[7] P. Sigmund and K.B. Winterbon, Nucl. Instr. and Meth. B12 (1985) 1.

[8] W.N. Lennard and H. Geissel, Nucl. Instr. and Meth. B27 (1987) 338.

[9] K.L. Brown et al, CERN 80-04 ; Superproton ; synchrotron Division ; 1980.

[10] P. Roussel, GEPL/05/83/58/AE/E

[11] R. Anne et al, Nucl. Instr. and Meth. A257 (1987) 215.

[12] Ch.O. Bacri, Thèse d'Université, IPNO-T-89-09.

[13] Ch.O. Bacri, IPNO-DRE-89-49.

Figure Captions

Figure 1 : Kinematical correlation between the emission angle and the energy loss in the target. Curves were computed for a 44 MeV/A ^{40}Ar beam. Vertical arrows indicate the grazing angle for the different targets. See text.

Figure 2 : 44 MeV/A ^{40}Ar beam probability distribution in the $B\rho$-θ plane after passing through a 8.1 mg/cm^2 ^{27}Al target. The correlation lines corresponding to proton and carbon contaminants are also drawn. Bold points keep the same meaning as in Fig. 1.

Figure 3 : The parallel to point telescopic setting mode of a spectrometer.

Figure 4 : Scheme of the telescopic mode use of a double magnetic spectrometer. D1 and D2 are two dipoles. Quadrupoles are not drawn.

Figure 5 : The LISE spectrometer in its "classical use".

Figure 6 : Evolution of the element matrix R_{11}, $10R_{12}$, R_{33}, $10R_{34}$ and R_{16} along LISE when used in a telescopic mode. The vertical plane is the upper part of the figure while the horizontal plane is represented in the lower part. The transport matrix at the intermediate dispersive plane are :

$$\begin{pmatrix} -0.40 & 0 & 2.065 \\ -17.396 & -2.461 & 8.636 \\ 0 & 0 & 1 \end{pmatrix}$$ in the horizontal plane, and

$$\begin{pmatrix} -6.893 & 0 \\ 22.54 & -0.132 \end{pmatrix}$$ in the vertical plane.

At the final plane, the matrix are

$$\begin{pmatrix} 0 & -0.177 & 0 \\ 5.633 & 0.661 & -2.22 \\ 0 & 0 & 1 \end{pmatrix}$$ and $$\begin{pmatrix} 0 & -0.177 \\ 5.653 & -0.168 \end{pmatrix}$$

The top and bottom limit lines of the figure correspond to a 10 cm amplitude in vertical and horizontal plane.

Figure 7 : A test pattern and its image in the horizontal and vertical planes (two different measurements). Two slits are separated by 8 mr while the central square corresponds to 16 mr (the test pattern was set 600 mm after the target).

Figure 8 : The angular shielding

a. ΔE - Time of flight plot for two excitation energy ranges : 38-12 MeV (left) and 38-8 MeV (right) in the inelastic channel, for the gold target.

b. Angular distribution of the ^{40}Ar time of flight range in the excitation range from 38 MeV down to 8 MeV.

c. ΔE-TOF plots for the angular ranges 0-3 mr and 3-7 mr.

Figure 9 : A sample of angular distribution. The continuous line is obtained with a window on the only time of flight while the full identification which requires ΔE is shopped by the granular structure of the solid state telescope. The dotted line represents the ^{38}Cl angular distribution while the dashed line represents the ^{40}Ar one.

Projectile	^{16}O				^{40}Ar				^{86}Kr			
Target	^{12}C		^{197}Au		^{12}C		^{197}Au		^{12}C		^{197}Au	
E (MeV/A)	25	80	25	80	25	80	25	80	25	80	25	80
θ^{gr}_{lab} (mr)	28,5	8,7	237	68	21,9	6,64	190,6	55,1	18	5,4	165	48
$1/l$gr (mr)	9,5	5,1	6,0	3,0	3,25	1,75	2,13	1,09	1,4	0,7	0,9	0,5

Table 1 : Grazing angle θ_{gr} and value of $1/l$gr ($l$gr : grazing angular momentum) given as an evaluation of the minimum size of an angular structure. All values are given in the laboratory system for different heavy-ion collisions at typical GANIL energies

		$\theta_{1/2}$ (mr)	θ_R (mr)
^{12}C	1 mg/cm^2	0.24	1.4
	10 mg/cm^2	1.05	7.2
	100 mg/cm^2	3.74	72
^{27}Al	1 mg/cm^2	0.3	1.8
	10 mg/cm^2	1.14	6.6
	100 mg/cm^2	5.1	54.7
^{197}Au	1 mg/cm^2	0.43	2.9
	10 mg/cm^2	2.03	13
	100 mg/cm^2	8.1	45

Table 2 : Half angle at half maximum $\theta_{1/2}$ for multiple scattering and value θ_R above which single Rutherford scattering is dominant (see text), corresponding to a 44 MeV/A ^{40}Ar beam impinging on different targets. All theses angles are expressed in mr in the laboratory frame.

	$x_i = y_i = 0,5$ cm $\theta_i = 9$mr ; $\varphi_i = 30$mr ; $\delta = 2,5$ %		$x_i = y_i = 0,1$ cm $\theta_i = 3$mr; $\varphi_i = 20$mr ; $\delta = 0,75$ %	
T_{ijk} ($\times 10^{-3}$)	corresponding Δx_f or Δy_f (cm)	corresponding $\Delta\theta$ or $\Delta\varphi$ (mr)	corresponding Δx_f or Δy_f (cm)	corresponding $\Delta\theta$ or $\Delta\varphi$ (mr)
$T_{111}=(x/x^2) = 15,4$	0,004	0,02	0,0002	0,0009
$T_{112}=(x/x\theta) = 5,73$	0,026	0,15	0,002	0,01
$T_{116}=(x/x\delta) = -362,4$	0,453	2,56	0,03	0,15
$T_{122}=(x/\theta^2) = 532,7\ 10^{-3}$	0,043	0,24	0,005	0,03
$T_{126}=(x/\theta\delta) = 55,9$	1,258	7,1	0,126	0,71
$T_{133}=(x/y^2) = 124$	0,031	0,17	0,001	0,007
$T_{134}=(x/y\varphi) = -4,964$	0,074	0,42	0,01	0,06
$T_{144}=(x/\varphi^2) = -1,38\ 10^{-3}$	0,0012	0,007	0,001	0,003
$T_{166}=(x/\delta^2) = 67,71$	0,423	2,39	0,04	0,22
$T_{313}=(y/xy) = -246,8$	0,062	0,35	0,002	0,011
$T_{314}=(y/x\varphi) = -4,926$	0,074	0,42	0,01	0,06
$T_{323}=(y/\theta y) = -36,74$	0,165	0,93	0,011	0,06
$T_{324}=(y/\theta\varphi) = -701,4\ 10^{-3}$	0,189	1,07	0,042	0,24
$T_{336}=(y/y\delta) = -702,7$	0,878	4,96	0,053	0,30
$T_{346}=(y/\varphi\delta) = -1,323$	0,099	0,56	0,02	0,11

Table 3 : Second order coefficients of the transport matrix and their effect in some typical cases. All dimensions correspond to half size (θ = 9 mr means $\theta = \pm$ 9 mr). The first case (column 2 and 3) is the limit case corresponding to the theoretical LISE acceptance (x_i, y_i arbitrary) ; the second case is close to the tested case.

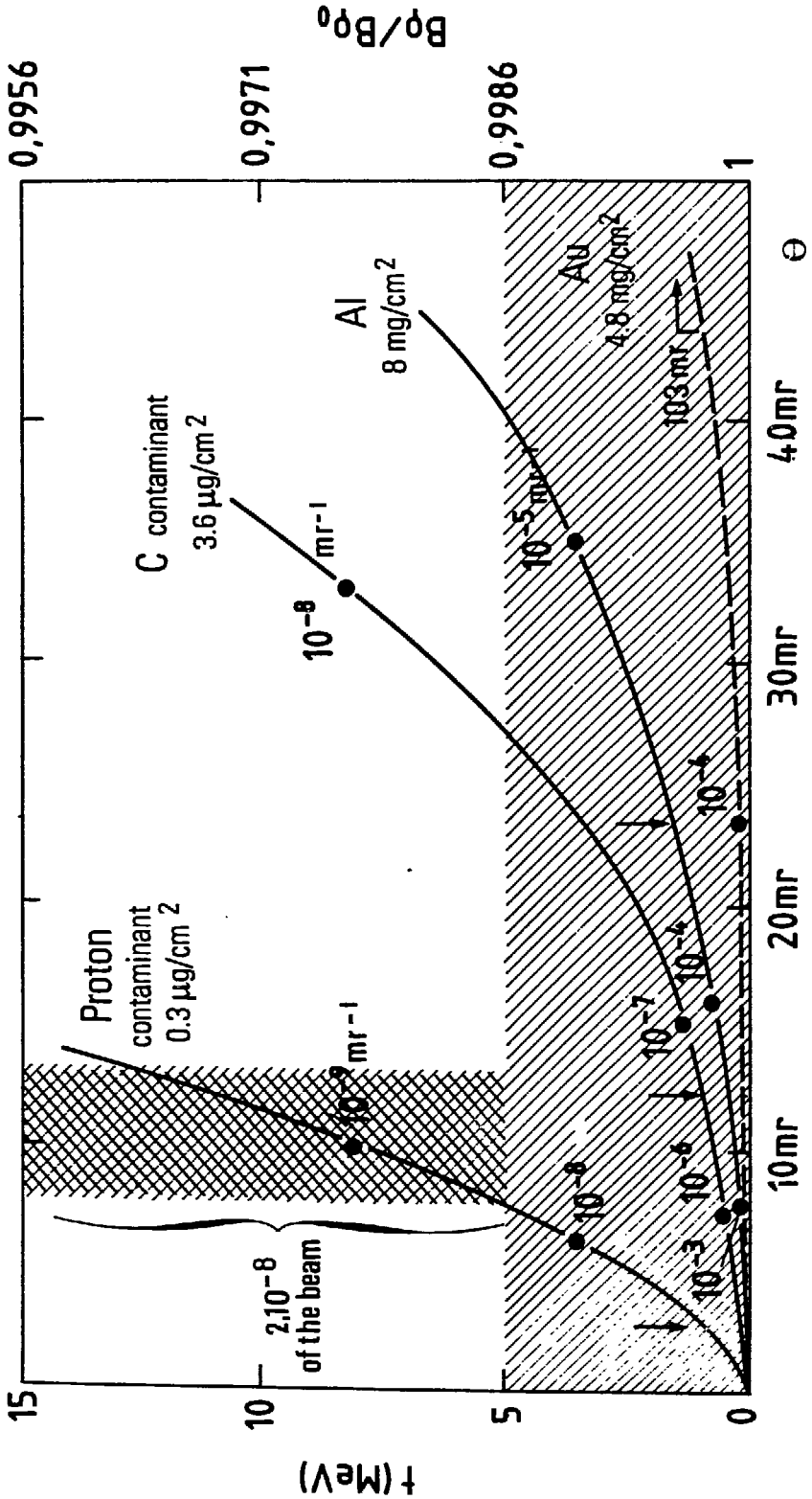
0,9956
0,9971
0,9986
1
Bρ/Bρ0
Θ
15
10
5
0
t (MeV)
10mr
20mr
30mr
40mr
Proton
contaminant
0.3 µg/cm 2
C contaminant
3.6 µg/cm 2
Al
8 mg/cm2
Au
4.8 mg/cm2
2.10-8
of the beam
10-8 mr-1
10-9 mr-1
10-5 mr-1
10-8
10-7
10-6
10-4
10-3
10-4
103 mr

Figure 1

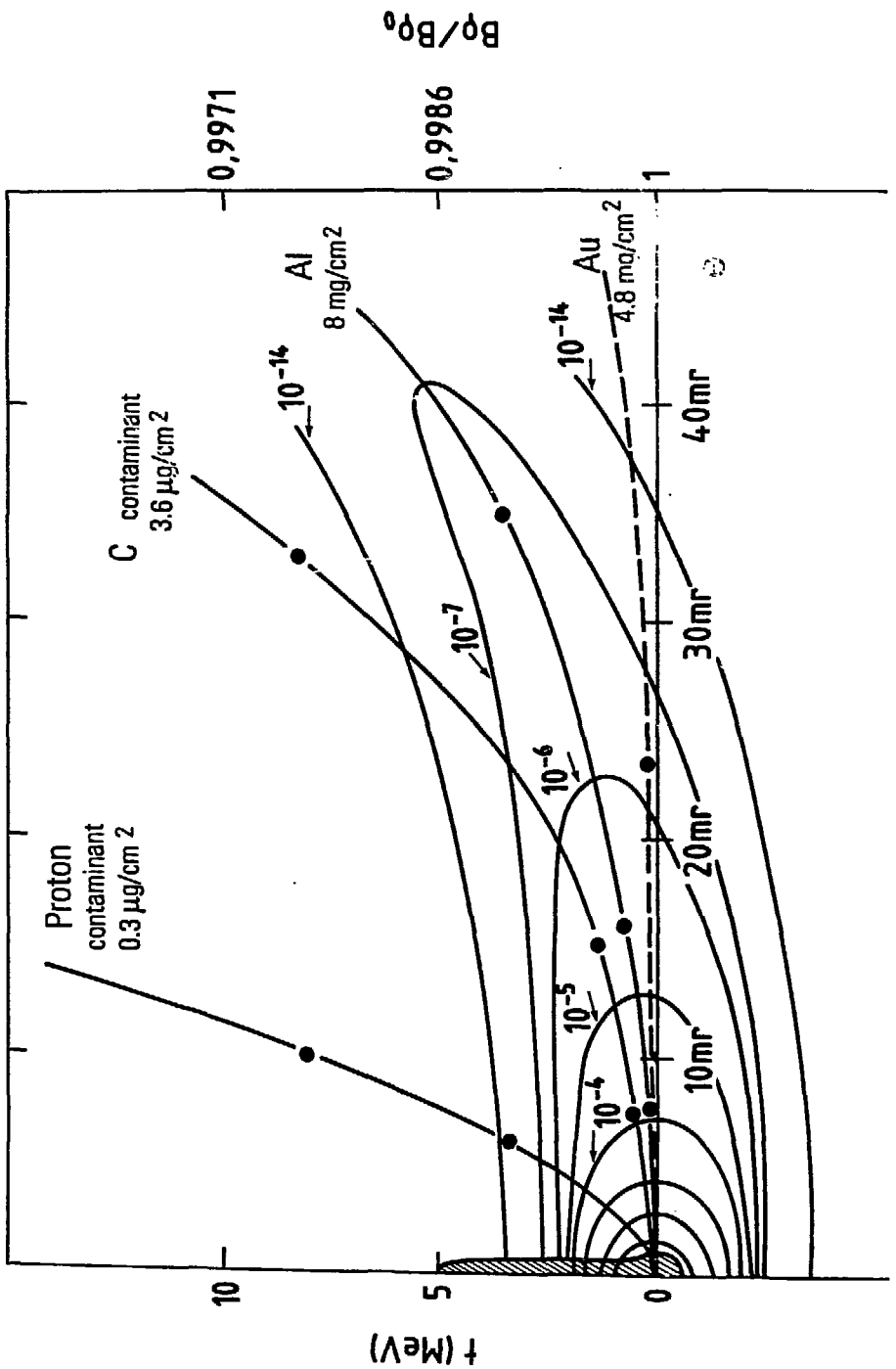
Bρ/Bρ₀
0,9971
0,9986
1
t (MeV)
10
5
0
Proton
contaminant
0.3 µg/cm²
C contaminant
3.6 µg/cm²
Al
8 mg/cm²
Au
4,8 mg/cm²
10⁻¹⁴
10⁻⁷
10⁻⁶
10⁻⁵
10⁻⁴
10⁻¹⁴
40mr
30mr
20mr
10mr

Figure 2

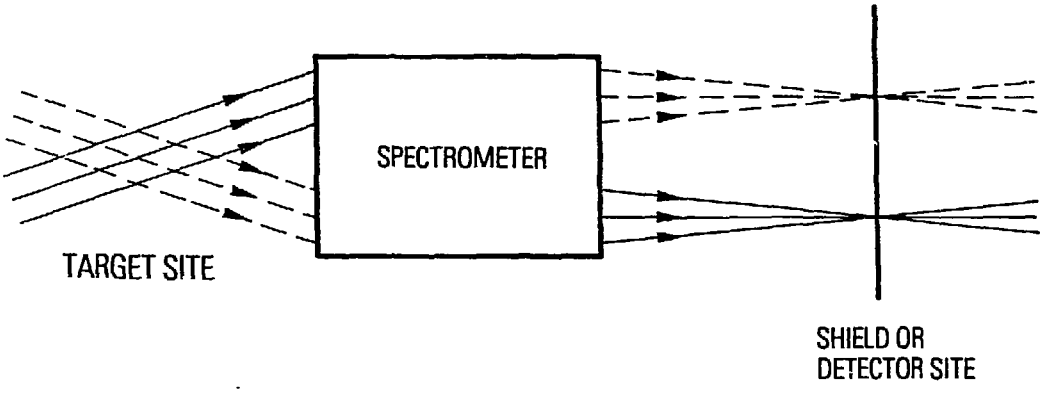

Figure 3

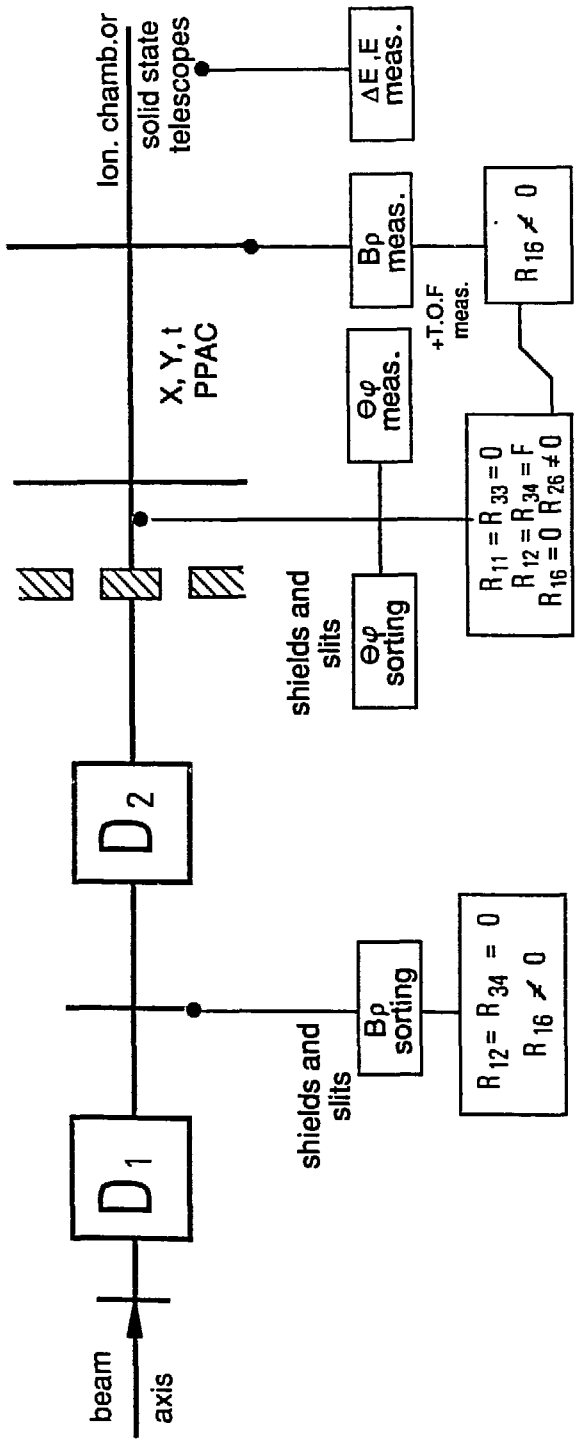
beam
axis
D1
D2
shields and
slits
Bρ
sorting
R12= R34 = 0
R16 ≠ 0
shields and
slits
eφ
sorting
R11 = R33 = 0
R12 = R34 = F
R16 = 0 R26 ≠ 0
X, Y, t
PPAC
eφ
meas.
Bρ
meas.
+T.O.F
meas.
R16 ≠ 0
Ion. chamb.or
solid state
telescopes
ΔE ,E
meas.

Figure 4

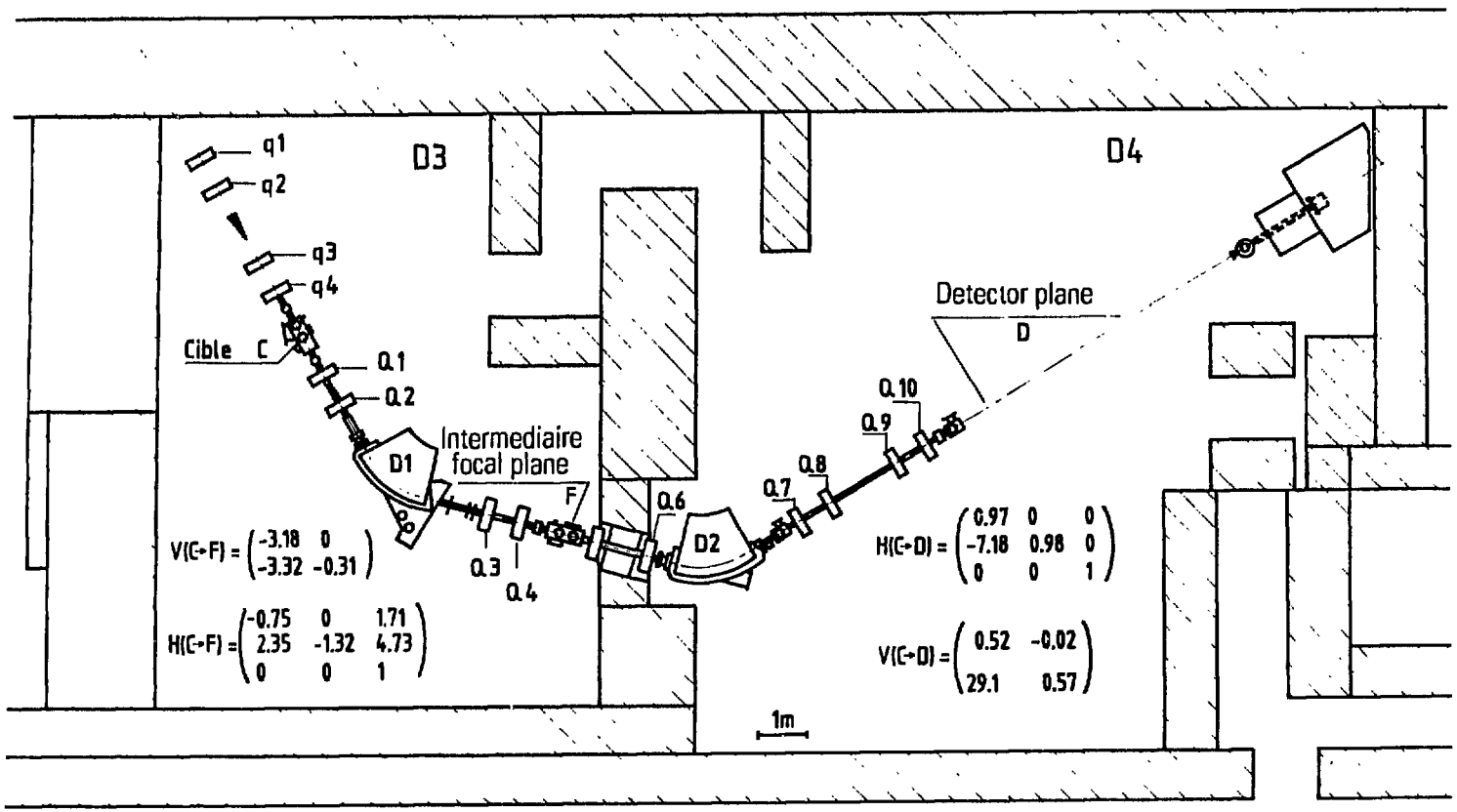
q1
q2
q3
q4
D3
D4
Cible C
Q1
Q2
D1
Intermediaire
focal plane
F
Q3
Q4
Q6
D2
Q7
Q8
Q9
Q10
Detector plane
D
V(C→F) = (-3.18 0 / -3.32 -0.31)
H(C→F) = (-0.75 0 1.71 / 2.35 -1.32 4.73 / 0 0 1)
H(C→D) = (0.97 0 0 / -7.18 0.98 0 / 0 0 1)
V(C→D) = (0.52 -0.02 / 29.1 0.57)
1m

Figure 5

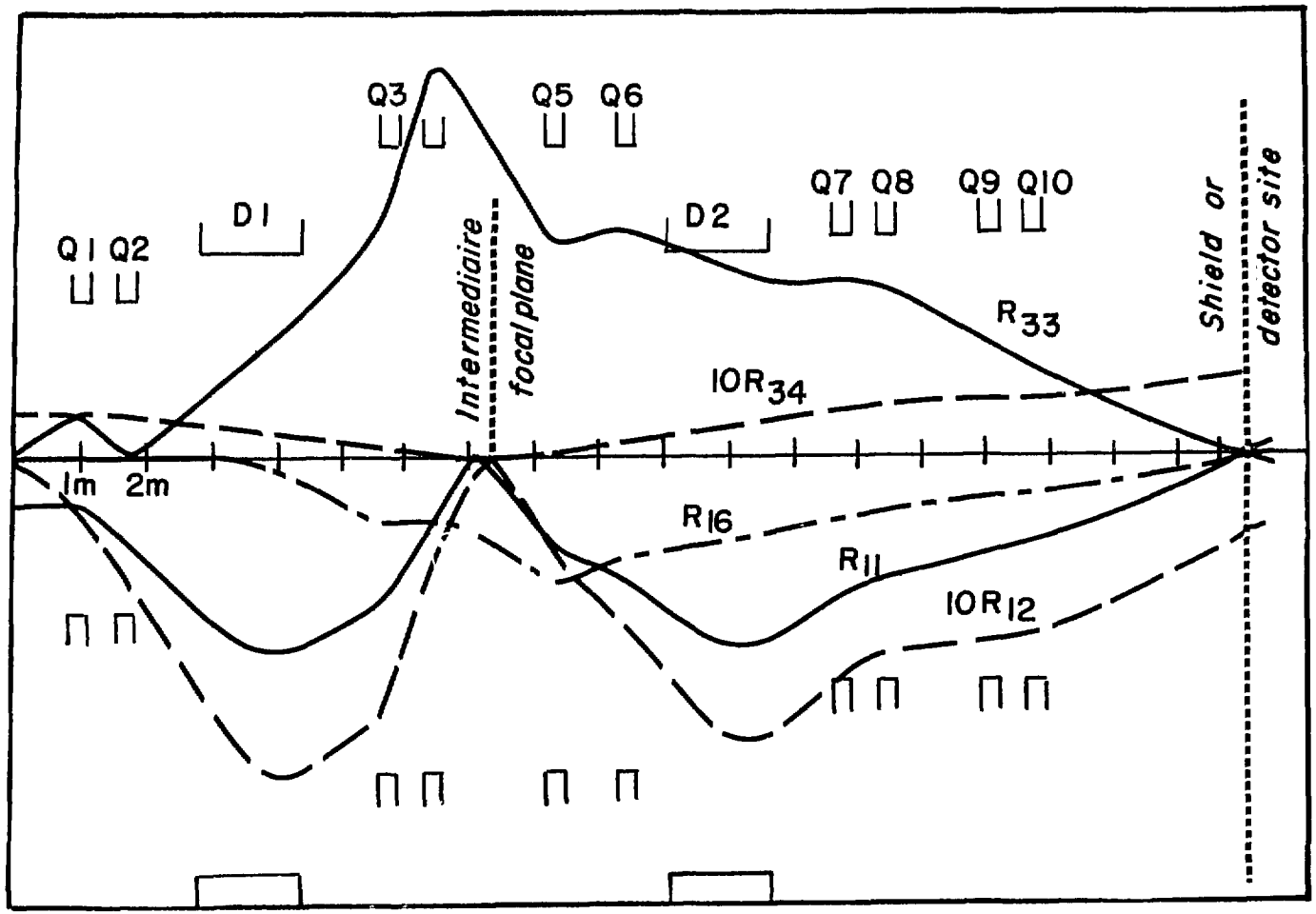
Q3
Q5 Q6
Q7 Q8
Q9 Q10
Q1 Q2
D1
D2
Intermediaire
focal plane
Shield or
detector site
R33
10R34
1m
2m
R16
R11
10R12

Figure 6

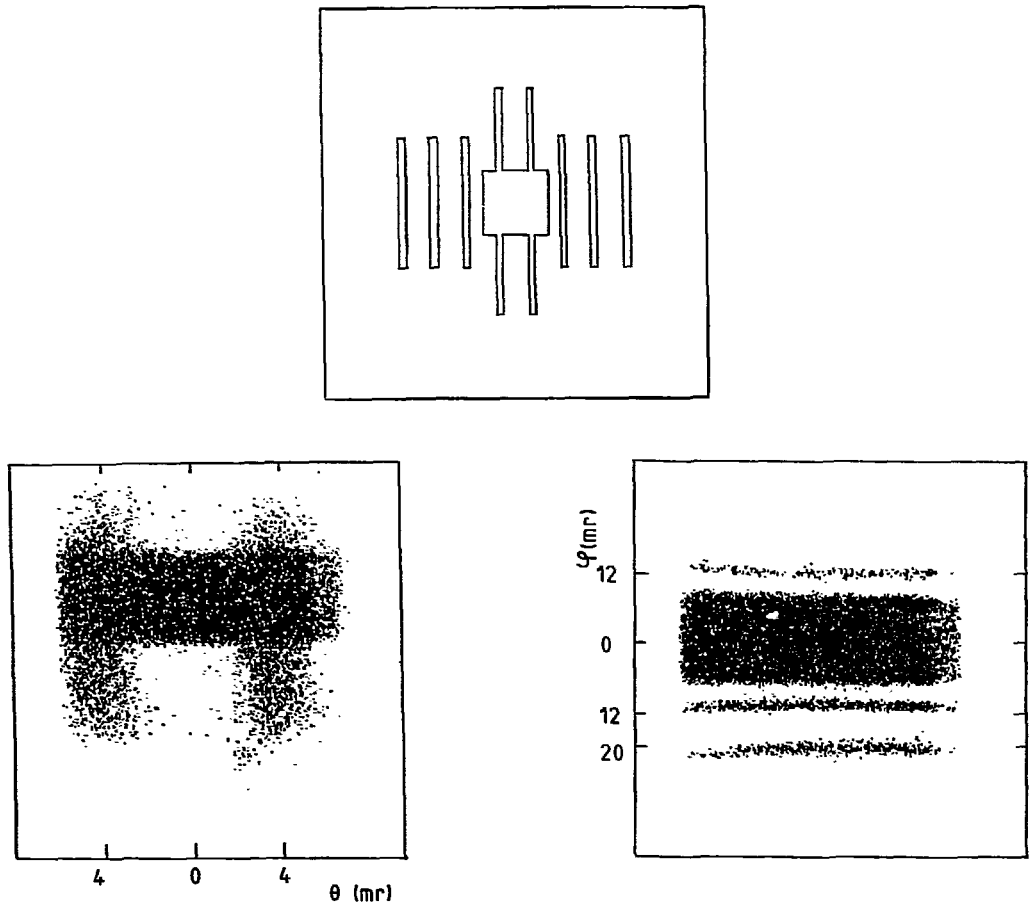

Figure 7

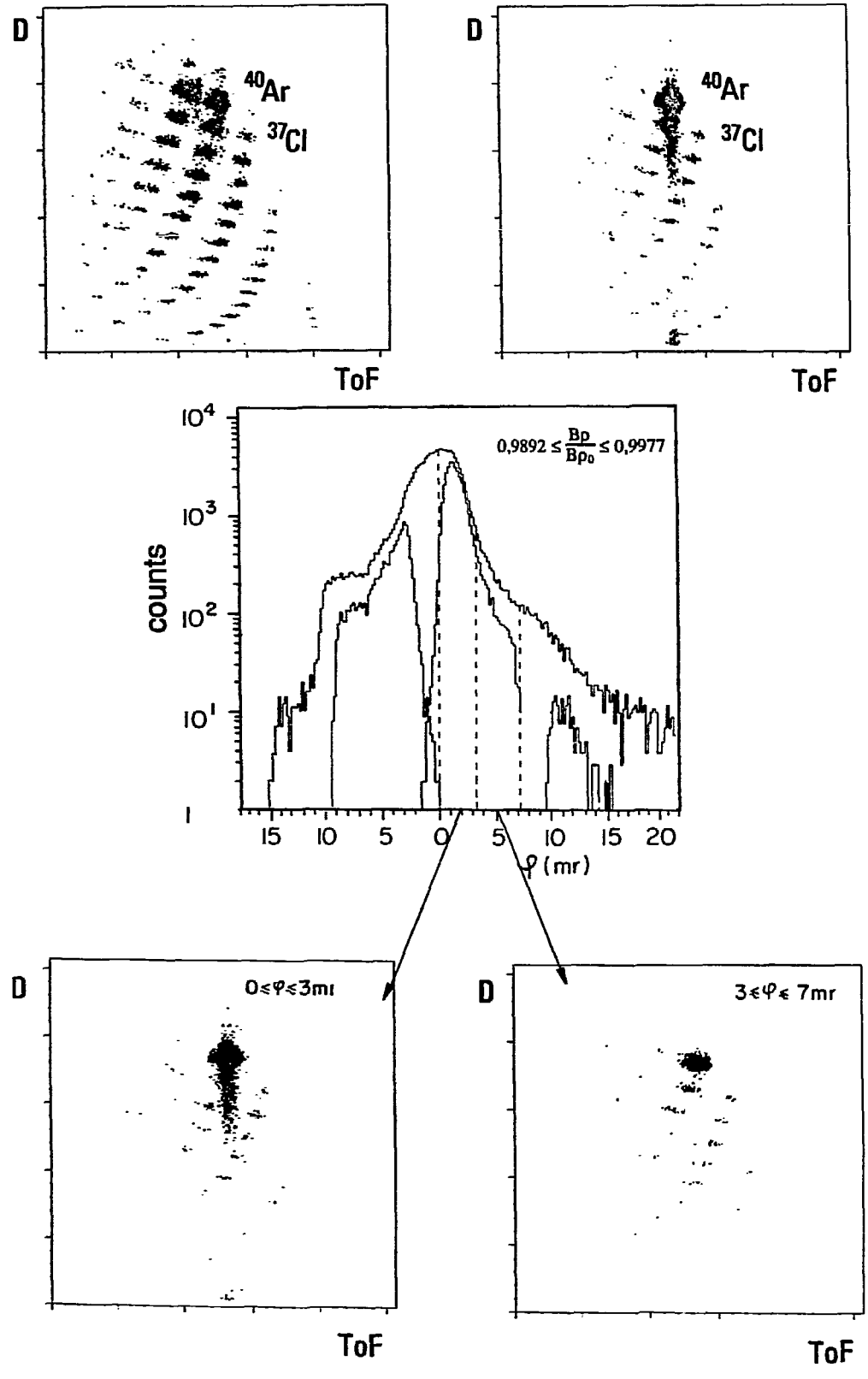
D
40Ar
37Cl
ToF
D
40Ar
37Cl
ToF
counts
10^4
10^3
10^2
10^1
1
$0{,}9892 \leq \frac{B\rho}{B\rho_0} \leq 0{,}9977$
15 10 5 0 5 10 15 20
φ (mr)
D
0≤φ≤3mr
ToF
D
3≤φ≤ 7mr
ToF

Figure 8

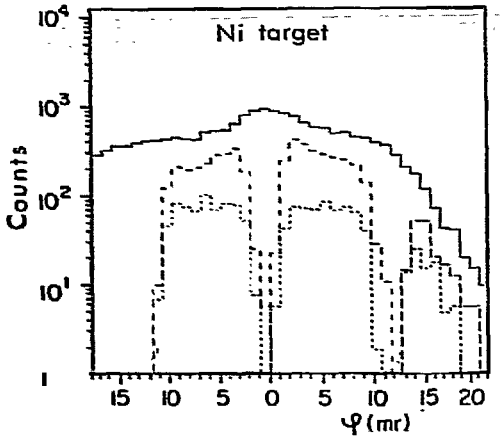

Figure 9